Electronic Supplementary Material (ESI) for Journal of Materials Chemistry A.
This journal is © The Royal Society of Chemistry 2018

Supplementary information:

1. **Experimental**

1.1 Electrolyte preparation

CGO pellets were formed from 10 mol% gadolinium doped cerium oxide powder (99.9%, Sigma Aldrich) milled with 3 wt% hydroxypropyl cellulose (Sigma-Aldrich, average molecular weight: 10,000) for 4 hours. Pellets were uniaxially pressed in a 12.5 mm diameter die under 3 tonnes before sintering at 1400 °C in air. Furnace ramp rates were 5 K min^{-1}. The sintered pellet had a diameter of 10 mm (area = 0.78 cm^2) and thickness 0.6 mm.

1.2 Composite cathode preparation

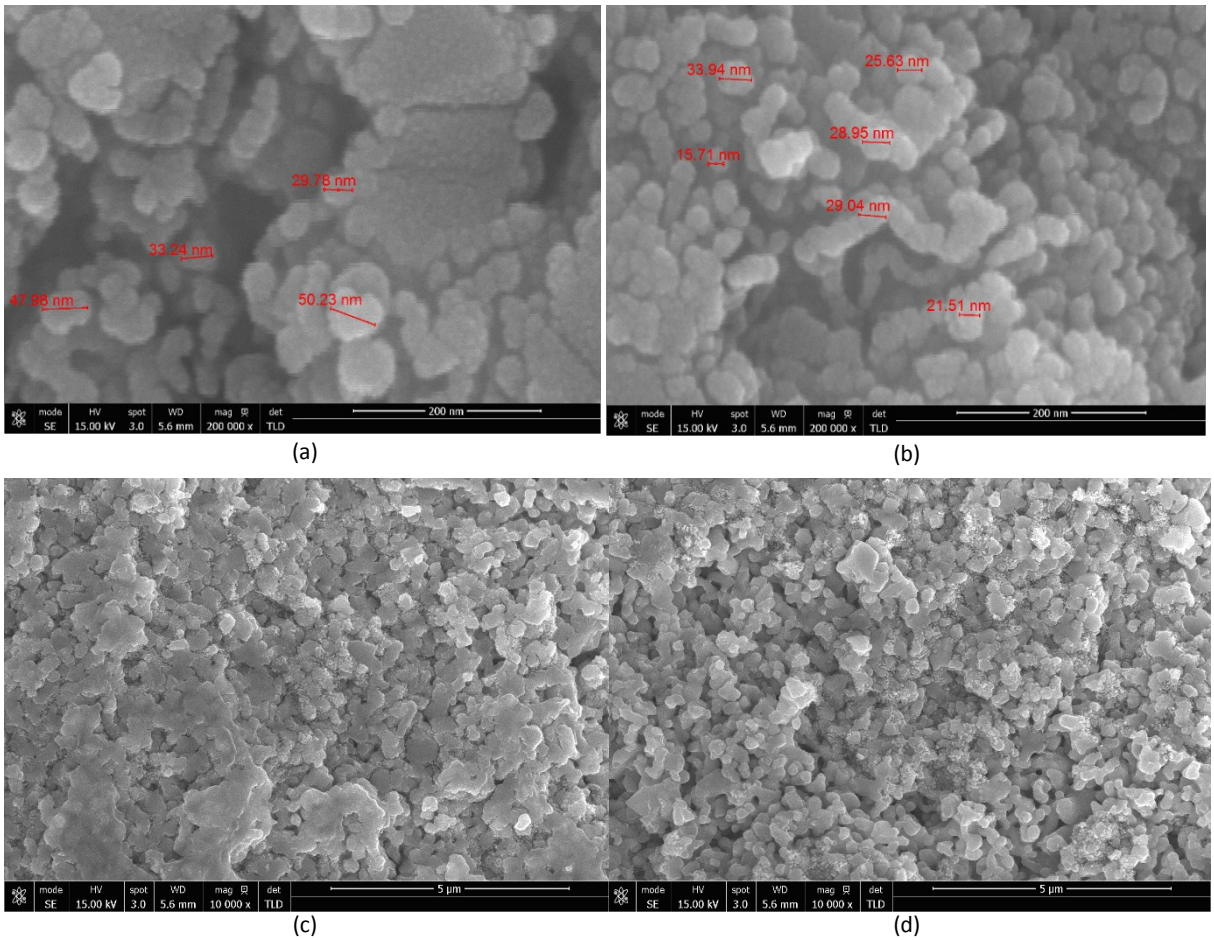

(a) (b)

(c) (d)

Fig. S1 High resolution SEM cross-sectional images of Co_xO_y:CGO (a, c) and CGO:Co_xO_y (b, d) infiltrated LSCF/CGO cathode electrodes.

Suspension inks was formed from commercial $La_{0.6}Sr_{0.4}Co_{0.2}Fe_{0.8}O_{3-\delta}$ (LSCF, Fuel Cell Materials), $Ce_{0.9}Gd_{0.1}O_{1.95}$ (CGO, Sigma-Aldrich), denoted further as CGO, and hydroxypropyl cellulose (Sigma-Aldrich) powders. Two stable primary inks, containing LSCF and CGO, respectively, were made from commercial ceramic powders. The powders were mixed with alpha-terpineol as a carrier and dispersant and ball milled with 3YSZ milling balls in a planetary mill. Hydroxypropyl cellulose was used as a polymeric dispersant for ink stabilisation. It provided steric stabilisation of the suspension and acted as a binder and a fugitive, promoting the formation of a porous scaffold. The rheology of the inks was adjusted to the viscosity range required for printing by varying the amounts of the diluting solvent. Methanol (reagent grade, Sigma-Aldrich) was chosen as a diluting solvent due to its high volatility, which enabled fast drying of the droplets. Terpineol (Sigma-Aldrich) was selected

as a low vapour pressure carrier, inducing Marangoni flows counteracting the formation of coffee-ring stains. It also played the role of a natural dispersant of the oxide particles and had excellent miscibility with the dispersant and the diluting solvent.

The composite cathode suspension ink was produced by mixing equal volumes of the individual LSCF and CGO suspension inks. The ink was filtered (3 µm glass fibre filter) before loading to prevent clogging of the print head. The cathodes were deposited with optimised printing parameters using an electromagnetically actuated nozzle (100 µm diameter ruby orifice, Domino Macrojet). A square array of drops with a 1 mm spacing was used with a 0.5 mm offset between print passes to prevent drop stacking. Six printing passes were used to deposit the cathodes. The samples were heated to ~120 °C between each pass. The cells were sintered in air at 1000 °C for 2 hours with heating and cooling rates of 5 K min^{-1}. The final cathode thickness was ~20 µm. SEM images of the infiltrated cathodes tested and aged at 650°C for 100h in air revieal CGO and CoxOy nanoparticles indistinguishable in shape and size (~ 20 nm) (see Fig. S1 (a-d).

The porosity of the reference and infiltrated electrodes after testing was estimated with image analysis of polished cross-sectional SEM images using ImageJ software. Images at five different locations per sample were analysed. Porosity values between 27 and 31 % were measured for all types of cathodes.

1.3 Solution ink synthesis & jetting

Both CGO and cobalt oxide (Co_xO_y) precursor solutions were synthesised for infiltrating symmetric cells. For the CGO ink a stoichiometric quantity of cerium nitrate hexahydrate (99.999%, Alfa Aesar) and gadolinium nitrate hexahydrate (99.9% Alfa Aesar) were added to absolute ethanol. Urea (>99.5%, Fisher Scientific) was added as a complexing agent (1:1.5 molar ratio Metals:Urea). The powders were dissolved with stirring and heating (40 °C). The solution was cooled to room temperature before being made up to 0.75 M total metal ion concentration with absolute ethanol and filtered (3 µm glass fibre filter) before storage. For the Co_xO_y ink cobalt nitrate hexahydrate (99%, VWR) was added to absolute ethanol. Urea was again used as a complexing agent (1:1.5 molar ratio Co:Urea). The powders were dissolved with stirring and the ink was made up to 0.75 M metal ion concentration with absolute ethanol before filtration and storage.

Table S1. Solution infiltration ink compositions and jetting parameters.

Ink	Cation concentration / M	Viscosity / cP	Opening time / µs	Pressure / mbar	Drop volume / nL	Drop velocity / ms^{-1}
CGO	0.75	4.7	240	225	58	2.3
Co_xO_y	0.75	4.3	230	225	62	1.6

An in-house drop visualisation system, consisting of a co-linear LED strobe and camera, was used to quantitatively assess the jetting of the solution inks. Analysis of the drop volumes and velocities and their dependence on the adjustable jetting parameters (opening time and fluid pressure) enabled the control of the jetting to achieve nearly identical molar loading of each ink into the porous cathodes. The ink properties and jetting parameters used are given in Table S1. The infiltration was performed at room temperature with intermediate heating to 150 °C between print passes. Five infiltration passes of one ink (CGO or Co_xO_y) were performed on each side before the samples were heated to 700 °C for 1 hour in air. Then the second ink was infiltrated using the same process. Sample CGO:Co_xO_y was infiltrated with the CGO solution ink first then the Co_xO_y solution ink. Sample Co_xO_y:CGO was infiltrated using the opposite sequence. A non-infiltrated reference cell was also tested.

1.4 Electrochemical characterization

All symmetrical cells were characterized by Two-electrode Electrochemical Impedance Spectroscopy (EIS) in order to determine their electrochemical performance. AC impedance measurements were performed with Autolab PGSTAT302N, Metrohm Autolab B.V. impedance analyser system. Gold was sputtered on each side of the symmetrical cells and gold wires were used for contacting the electrodes. The EIS scans with AC amplitude of 10 mV were conducted at temperatures ranging from 500°C to 700oC at 50°C intervals in ambient air. Impedance measurements were performed from 0.01 Hz to 100 kHz after 15 min of thermal equilibration at each temperature. Samples were tested in their initial as-prepared state and again after a total effective aging of 100 hours at 650 °C. Nyquist plots at different test temperatures for all samples are presented in Fig. S2. Superimposed experimental and fitted with an equivalent circuit (see inset) spectra are presented in Fig. S3.

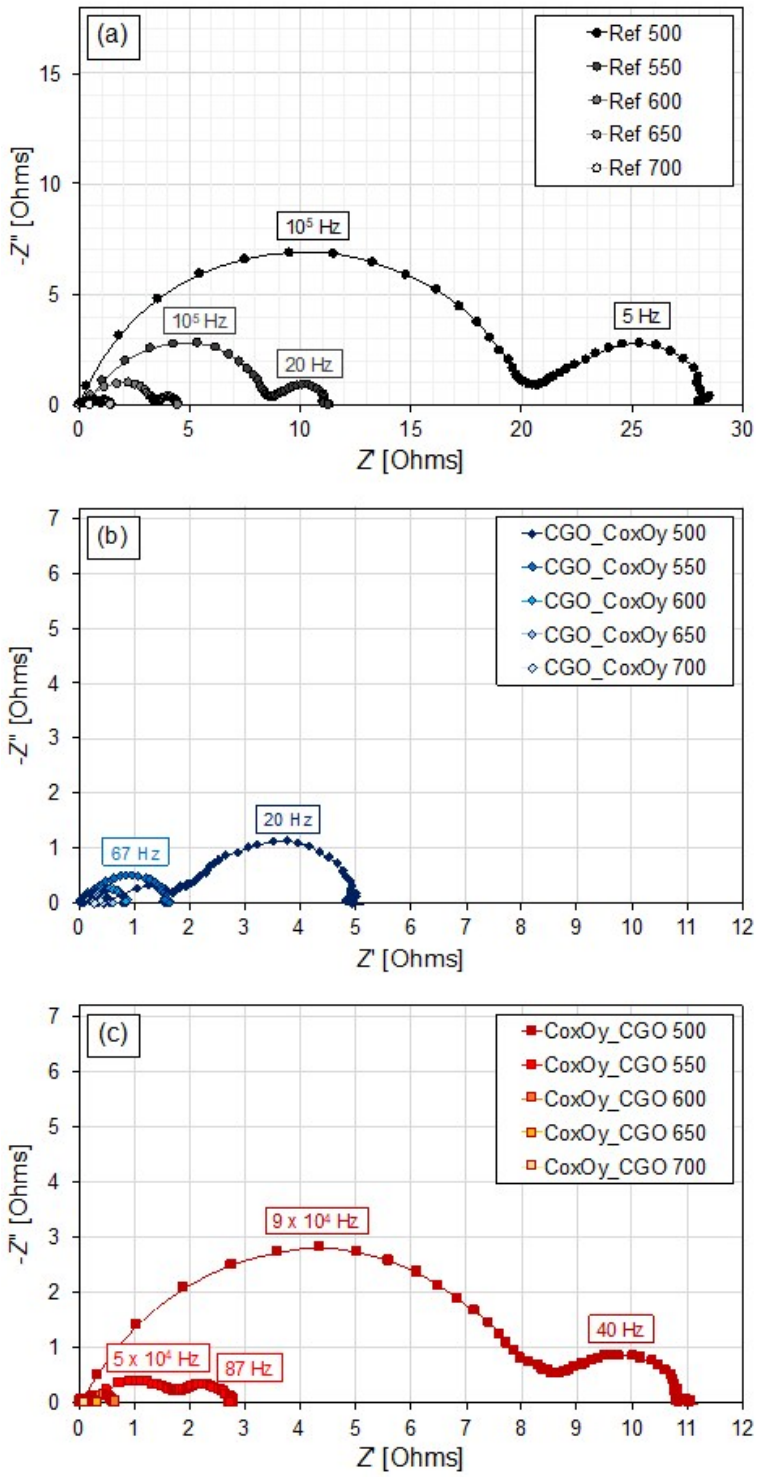

Fig. S2. Nyquist plots at different test temperatures for (a) Reference sample, (b) sample CGO:Co_xO_y and (c) sample Co_xO_y:CGO. Results for non-aged samples. Note the difference in scale between (a) and (b), (c).

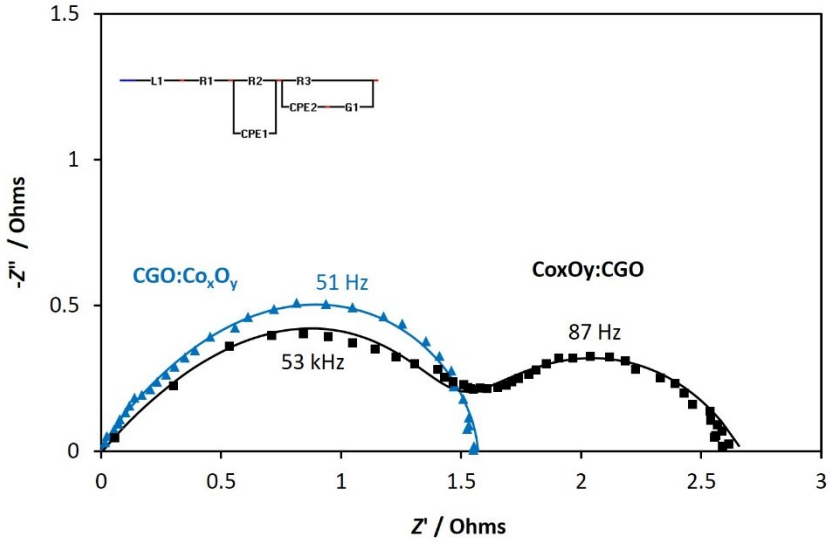

Fig. S3 Nyquist plots at 550°C for samples CGO:Co_xO_y and Co_xO_y:CGO (symbols) and the best fit to the equivalent circuit shown in the inset of Fig. S3 (solid lines).

2. Characterization

2.1 XPS

Fig. S3 shows the XPS survey spectrum comparing the LSCF/CGO cathode and the dual infiltrated CGO:Co_xO_y and Co_xO_y:CGO on a LSCF/CGO cathode. The measurements were performed after aging at 650°C in air for 100 hrs. As expected, the cathode with CGO infiltrated second shows an intense Ce 3*d* signal and a weaker Co 2*p* signal, and vice versa for the sample when Co_xO_y is infiltrated after CGO.

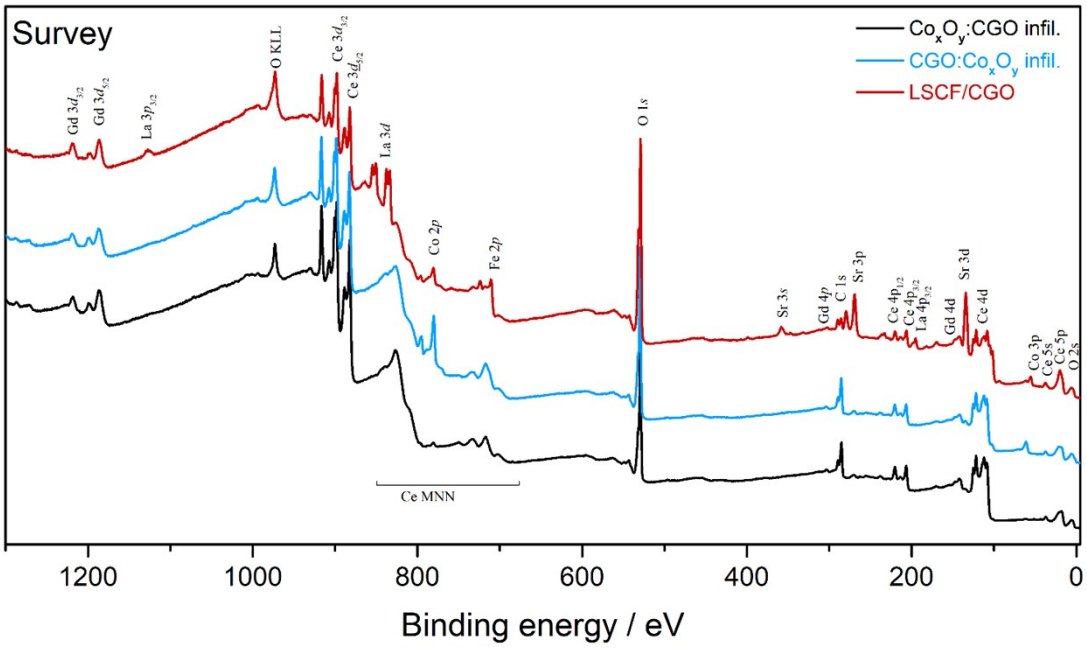

Fig. S4. Survey spectra of the LSCF/CGO sample (red), dual infiltrated Co_xO_y:CGO in LSCF/CGO (black) and dual infiltrated CGO:Co_xO_y in LSCF/CGO (blue).

Fig. S4 show the Ce/G*d* 4*d* core level spectra. A shift towards higher binding energy (0.6 eV) is observed for both dual infiltrated samples. This increase in B.E. position for both dual infiltrated samples could be due to a shift of the Fermi level because of the increasing concentration of Ce^{3+} states present above the main valence band edge, although this is complicated by the presence of Co(III) states above the valence band maximum (VBM). The intensity and structure in the region of the Ce 4*d* core level (105-125eV) and of the Gd 4*d* core level (138-152 eV) has also been influenced by the dual infiltration. The changes observed in the region 100-108 eV are due to two factors, firstly the loss of signal of La 4*d* from the LSCF substrate and secondly an increase of the Co 3*s* signal after the infiltration of Co_xO_y nanoparticles. The Gd 4*d* core level (137.5-152 eV) in the LSCF/CGO sample is more intense than that of both dual infiltrated samples with an atomic ratio of the Gd 4*d* : Ce 3*d* of 15:85 for the LSCF/CGO sample and 10:90 for the two dual infiltrated samples.

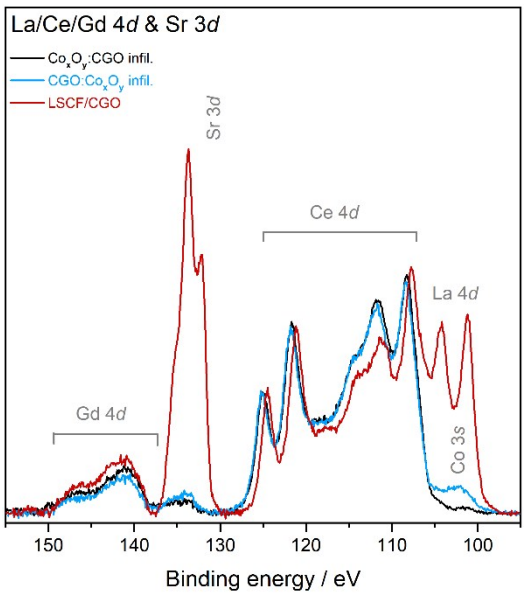

Fig. S5. La/Ce/Gd 4*d* and Sr 3*d* core level spectra of the LSCF/CGO sample (red), dual infiltrated Co_xO_y:CGO in LSCF/CGO (black) and dual infiltrated CGO:Co_xO_y in LSCF/CGO (blue).

The Ce 3*d* core level in Fig S5 shows mainly a cerium doped oxide in the +4 oxidation state, with the characteristic three doublets contribution namely (v,u), (v'',u''), (v''',u''') at positions in good agreement with literature[1]. The Ce 3*d* of the LSCF/CGO sample differs from the dual infiltrated samples at the position of the two doublets from the +3 oxidation state of the cerium oxide. This is in good agreement with the observation made on the amount of gadolinium in the LSCF/CGO sample as doping the cerium oxide with gadolinium forms a more stoichiometric cerium oxide due to the critical ionic radius r_c of the Gd(III) ion (r_c = 1.05 Å) being very close to the ionic radius of the Ce(IV) ion (r_c = 1.038 Å)[2]. Also, the fact that the doped cerium oxide infiltrated on the LSCF/CGO is formed of nanoparticles of size of about 20 nm, which has been found to enhance the amount of Ce(III) at the surface of infiltrated samples[3,4,5]. Fig S7 shows the O 1*s* core level spectra of all samples. It reveals a shift for the O 1s core level attributed to the difference in B.E. between the O 1s O- Ce (529.3 eV)[6,7,8] and O-La (528.7 eV)[9,10].

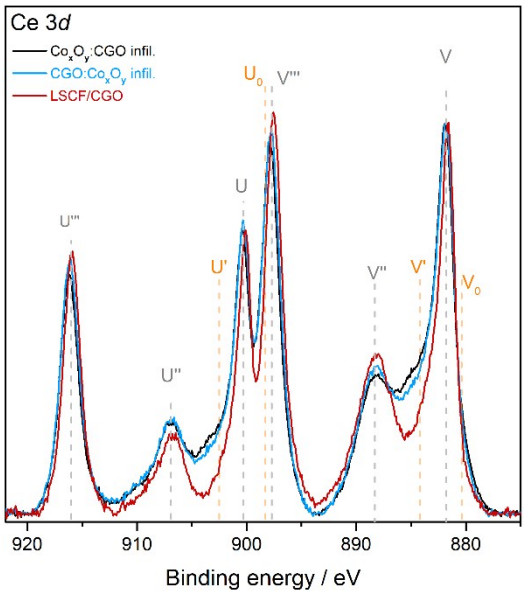

Fig. S6. Ce 3*d* core level spectra of the LSCF/CGO sample (red), dual infiltrated Co_xO_y:CGO in LSCF/CGO (black) and dual infiltrated CGO:Co_xO_y in LSCF/CGO (blue).

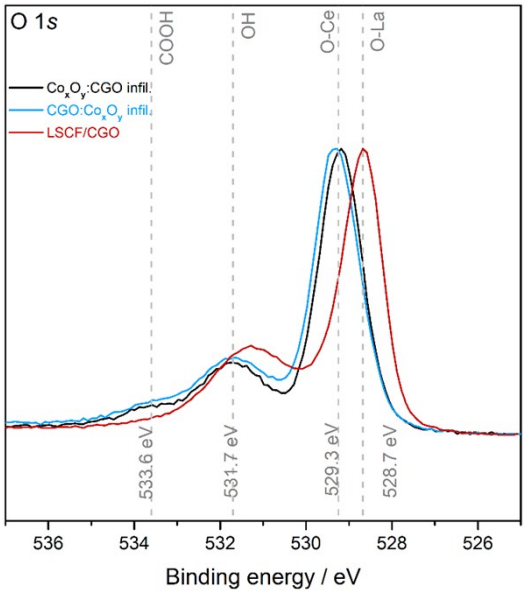

Fig. S7. O 1*s* core level spectra of the LSCF/CGO sample (red), dual infiltrated Co_xO_y:CGO in LSCF/CGO (black) and dual infiltrated CGO:Co_xO_y in LSCF/CGO (blue).

Table S2. Quantification results obtained from the core level XPS data.

	Ref		CGO_Co_xO_y		Co_xO_y_CGO	
	Peak BE / eV	Atomic %	Peak BE / eV	Atomic %	Peak BE / eV	Atomic %
O 1*s* O-La	528.6	49	-	-	-	-
O 1*s* O-Ce	529.3	12	529.5	66	529.2	68
Ce 3*d*	881.6	12	882.4	20	882.1	27
Sr 3*d*	133.7	10	133.7	1	133.7	0.5
Co 2*p*	780.1	8	780.0	12	780.4	2
La 3*d*5/2	833.1	6	-	-	-	-
Gd 4*d*	141.9	2	141.4	2	141.3	3

Table S3. Atomic ratios determined by XPS spectra for reference and infiltrated LSCF/CGO cathodes.

	Ref	CGO_Co_xO_y	Co_xO_y_CGO
Ce 3*d* : Gd 4*d*	85:15	93:7	91:9
Sr 3*d* : Ce 3*d*	45:55	3:97	2:98

2.2 In-situ Raman spectroscopy

High temperature Raman spectroscopy for all samples measured during heating and cooling cycle from room temperature to 700°C is presented in Fig. S5.

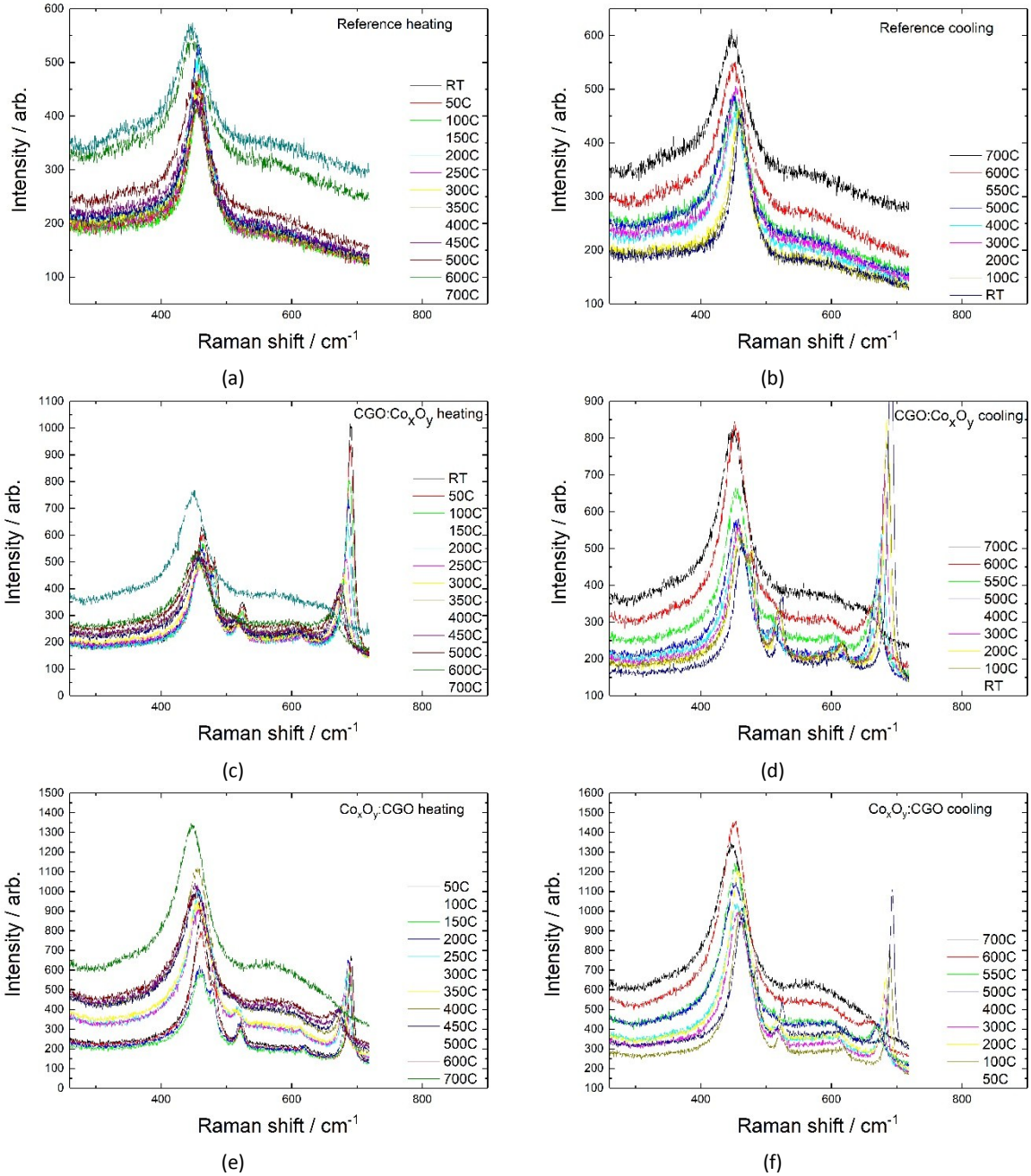

Fig. S8. In situ Raman spectroscopy (heating and cooling) for the reference cathode (a) and (b); CGO:Co_xO_y infiltrated cathode (c) and (d); Co_xO_y:CGO infiltrated cathode (e) and (f).

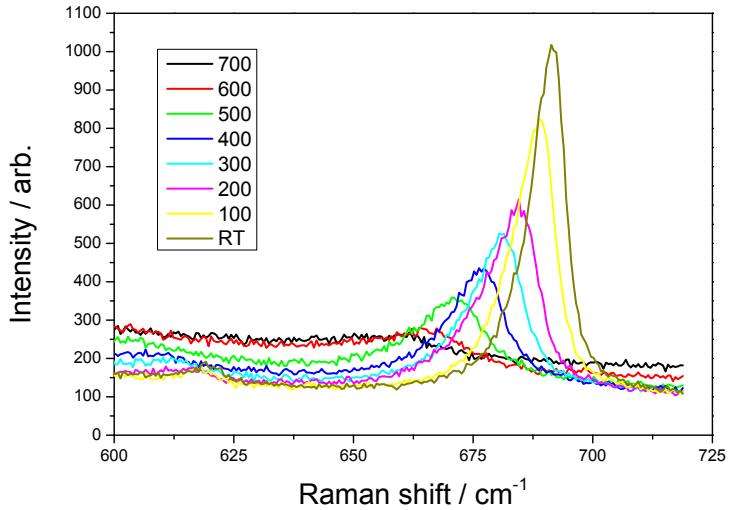

Fig. S9. In situ Raman spectroscopy (cooling) for a thick layer of Co_xO_y printed on to a dense CGO pellet.

Table S4: Peak positions and FWHMs for ~450cm^{-1} CGO and ~685cm^{-1} Co_3O_4 peaks before and after heat cycle for both samples.

	CGO peak		Co_3O_4 peak	
	Position cm^{-1}	FWHM cm^{-1}	Position cm^{-1}	FWHM cm^{-1}
CGO:Co_xO_y Before	458.6	24.7	686.8	12.8
CGO:Co_xO_y After	460.9	27.8	687.0	13.0
Co_xO_y:CGO Before	458.1	29.4	688.0	9.9
Co_xO_y:CGO After	460.1	27.9	689.1	9.3

Table S5: I_{Co3O4}/I_{CGO} area ratios at 550°C at t = 0 and t = 12 hours.

	I_{Co3O4}/I_{CGO} At 550°C t=0	I_{Co3O4}/I_{CGO} At 550°C t=12 hours	Change in I_{Co3O4}/I_{CGO}
CGO:Co_xO_y	0.268	0.274	1.02x
Co_xO_y:CGO	0.0027	0.0021	0.78x

Table S6: I_{Co3O4}/I_{CGO} area ratio before and after heat cycle for both samples.

	I_{Co3O4}/I_{CGO} Before Heat Cycle	I_{Co3O4}/I_{CGO} After Heat Cycle	Change in I_{Co3O4}/I_{CGO}
CGO:Co_xO_y	0.827	1.575	1.9x
Co_xO_y:CGO	0.055	0.237	4.3x

[1] B. P. Burroughs, A. Hamnett, A. F. Orchard, and G. Thornton, *J. Chem. Soc., Dalt. Trans.,* 1976, 1686.
[2] R. D. Shannon, *Acta Crystallogr. Sect. A*, 1976, **32**(5), 751.
[3] C. Sun, H. Li and L. Chen, *Energy Environ. Sci.*, 2012**, 5**, 8475.
[4] S. Tsunekawa, R. Sahara, Y. Kawazoe, and K. Ishikawa, *Appl. Surf. Sci.*, 1999, **152**(1), 53.
[5] S. Deshpande, S. Patil, S. V. Kuchibhatla, and S. Seal, *Appl. Phys. Lett.*, 2005, 87(13), 1.
[6] D. Barreca, G. A. Battiston, R. Gerbasi, and E. Tondello, *Surf. Sci. Spectra*, 2000, **7**(4), 297.

[7] M. Alexandrou and R. M. Nix, *Surf. Sci.*, 1994, **321**, 47.
[8] G. S. Herman, Y. J. Kim, S. A. Chambers, and C. H. F. Peden, *Langmuir*, 1999, **15**(11), 3993.
[9] P. A. W. Van Der Heide, *Surf. Interface Anal.*, 2002, **33**(5), 414.
[10] A. Galenda, M. M. Natile, V. Krishnan, H. Bertagnolli, and A. Glisenti, *Chem. Mater.*, 2000, **19**(11), 2796.